A type of robust superlattice type-I Weyl semimetals with four Weyl nodes

Lijun Meng✉, Jiafang Wu, Jianxin Zhong and Rudolf A Römer✉

Hunan Key Laboratory for Micro-Nano Energy Materials and Devices, Hunan, People's Republic of China

Faculty of Materials and Optoelectronic Physics, Xiangtan University, Xiangtan 411105, Hunan, People's Republic of China

Department of Physics, University of Warwick, Coventry, CV4 7AL, United Kingdom

Abstract

We investigate the topological properties of the Janus superlattices WTeS and WTeSe by first-principles methods and Wannier-based tight-binding Hamiltonians. The thermal stability of the Janus structures is checked by first-principles molecular dynamics. The topological properties are identified through node chirality, surface states and surface Fermi arcs. Our calculations reveal that both WTeS and WTeSe are Type-I Weyl semimetals with only four Weyl nodes in the Brillouin zone, which is a minimal number in a time reversal symmetry system. This small number of Weyl nodes makes them an excellent platform to study their topological properties experimentally. The Weyl nodes are located in four different quadrants of the Brillouin zone and consequently the separation of Weyl points in reciprocal space, and the length of Fermi arc, is of the order of the magnitude of the reciprocal lattice vector $|G_z|$ as might be easily observed in experiment. The Weyl nodes have approximately the same energy below the Fermi level and are hence accessible by conventional ARPES. In addition, under external strain, the Weyl semimetal state is more robust than the sister compounds T_d-WTe_2/$MoTe_2$. Our findings are important to explore Weyl fermion physics and useful for realizing possible applications of Weyl semimetal materials in future topological electronic devices.

Keywords

Topological Weyl semimetal; Janus structure; transition metal chalcogenides; Fermi arc; first-principles calculations

1. Introduction

Over the past decade, we have learned that materials can be classified into different categories according to the topology of their band structures [1-8]. Recently, a large number of topological materials have been discovered by symmetry indicator and topological quantum chemical methods [5-7, 9, 10]. Topological insulators (TIs) are insulators with inversion-band structure caused by strong spin-orbit coupling (SOC) which differ from the band insulators [11, 12]. The inverted bulk band gives rise to a

✉ The corresponding author Email: ljmeng@xtu.edu.cn

✉ The corresponding author Email: R.Roemer@warwick.ac.uk

robust metallic surface state and exhibits a Dirac cone-type dispersion in which spin and momentum are locked-in and perpendicular to each other [11]. Topological semimetals (TSMs) are another class of topological materials which also possess exotic surface states [1, 4, 13, 14]. Topological Dirac semimetal and Weyl semimetal were the first two topological semimetal materials characterized by four- and two-fold degeneracy of their touching points, respectively. Unlike in standard Lorentz invariant field theory, materials physics has two distinct types of Weyl fermions, classified according to whether the Lorentz symmetry is broken, and hence Weyl semimetals (WSMs): Type I and Type II WSM [1, 2, 13-17]. Type I Weyl semimetal including pyrochlore iridates [14], $HgCr_2Se_4$ [13], TaAs family [1] possesses the Lorentz symmetry of its Weyl cone which was predicted theoretically and identified experimentally [1, 8, 13, 14]. The Weyl cone exhibits an isotropic Fermi velocity and leads to a remarkable abnormal chirality and magnetic resistance under parallel electric and magnetic fields [15, 18]. The type II WSM hosts a titled Weyl cone with broken Lorentz symmetry and the Weyl nodes act as the touching points at the boundary between electron and hole pockets. The typical Type II WSM was discovered in transition metal dichalcogenides WTe_2, $MoTe_2$ and their alloy $Mo_{1-x}W_xTe_2$ [2, 3, 19, 20]. Other Type II WSM materials were also predicted theoretically and identified experimentally in recent year [21, 22]. The type-II WSMs are predicted to exhibit an open Fermi surface that results in an anisotropic chiral anomaly and a negative magnetoresistance effect which are very different from their type-I counterparts [2, 23, 24].

The representatives of type-II WSMs materials considered to date are the orthorhombic low temperature phases (T_d) of WTe_2 [2, 15], $MoTe_2$ [3, 19] and their alloy $Mo_{1-x}W_xTe_2$ [20, 25]. Eight type-II Weyl points (WPs) appear in WTe_2 ($MoTe_2$) formed by the crossing of the valence band (VB) and conduction band (CB) in the k_z=0 plane. However, due to the small separation of the WPs, it is still a challenging task to experimentally confirm the type-II Weyl phase in WTe_2 and $MoTe_2$. The identification of materials with *stable and easily observable* WPs thus sets an important problem in the study of this new topological phase. One crucial challenge is that the Weyl nodes and topological Fermi arcs are predicted to feature entirely above the Fermi level, so that they are inaccessible for conventional angle-resolved photoemission spectroscopy (ARPES) [26].

Tailoring the chemical composition in materials to form alloy structures is an efficient route to enhancing their physical and chemical properties [20, 25, 27-31]. Recently, Lu et al. have reported a synthetic strategy to grow a Janus MoSSe monolayer by fully replacing the top-layer S with Se atoms in MoS_2 [27]. Similar structures were also theoretically proposed in recent studies for other TMD materials [27-31]. Their synthetic route provides extra degrees of freedom to obtain new materials due to many possible way of substituting atoms between layers for layered TMD materials. The broken out-of plane mirror symmetry in a Janus monolayer leads to new exotic electronic properties compared to traditional sandwiched structures. The Janus structures of TMD have been widely investigated with regards to their electronic, optical and catalytic properties [27-30]. The new-developed method paves a way to

View Article Online
DOI: 10.1039/C9NR04551A

synthesize Janus-like superlattice structures of TMDs MXY (M=Mo,W,Nb,Ta; X, Y=S,Se,Te) in different crystal phases.

In the present paper, we theoretically construct two Janus-like superlattice structures in the T_d phase for WTeS and WTeSe systems. The structures are fully relaxed considering both lattice parameters and atom positions using a van der Waals (vdW) corrected first-principles method. The thermal stabilities of the optimized structures are checked by first-principles molecular dynamics (FPMD) up to a duration of 10*ps* and using a 3×3 supercell. Then the electronic bands of the optimized structures are calculated by employing a first-principles method with SOC and Wannier-based tight-binding Hamiltonian. The topological electronic properties including the distribution of Weyl nodes, surface state and surface Fermi arc for the optimized Janus structures are analyzed using tight-binding Hamiltonians obtained by projecting Bloch orbits to atomic like Wannier orbits. The two-dimensional (2D) band dispersion around Weyl nodes and the chirality of Weyl points are analyzed. The effect of uniaxial strain along *c* axis on the topological properties is considered to check the robustness of topological state.

2. Models and Methods

In the present work, we construct two Janus superlattice models in the T_d phase by completely replacing the Te atom layer with an S/Se atom layer in the standard T_d phase WTe_2 as shown in Fig.1 (*a*). The pristine T_d phase displays a *y-z* plane mirror symmetry m_{yz} and a glide plane g_{xz} including a reflection in the *x-z* plane followed by a (0.5, 0, 0.5) translation. Note that the T_d phase structure has broken the space inversion symmetry. This results in a twofold degeneracy of Weyl points in T_d-WTe_2 and T_d-$MoTe_2$ materials [2-4, 19]. The bottom/top Te layers in the two monolayers are substituted by S layers and form a Janus superlattice configuration. The structure retains its original *y-z* plane mirror symmetry, but breaks glide plane g_{xz} symmetry. Two initial structures with the primitive lattice parameters of T_d-WTe_2 are fully relaxed which allows simultaneously optimizing the positions of atoms and lattice parameters of the unit cell as given in Table I. As a result, the lattice parameters change slightly and give rise to a structural transition from pristine orthorhombic T_d-phase to a monoclinic phase. For example, the parameters *a*, *b* and *c* demonstrate a compression about 0.16Å, 0.22Å and 0.89Å, respectively, for WTeS. The angle α in the monoclinic phase demonstrates a deviation compared to the standard T_d-phase with angle α=90°. The α angles for both structures are 91.81° and 91.20°, respectively, and lead to a slightly broken g_{xz} symmetry. As a consequence, the distribution and the number of Weyl points are distinct from the pristine T_d-WTe_2 system.

In order to confirm the thermal stability of the optimized structures, we conduct a long-time FPMD calculation based on 3×3 supercell for two optimized structures at temperature 300K. A velocity Verlet algorithm, with time step of 2*fs* and *NVT* ensemble, was adopted. The temperature and the total energy of WTeS/Se exhibits thermal fluctuation around average values up to 10*ps* as shown in Fig.1(*c*)-(*f*). Additionally, we also presented the phonon dispersions along high symmetry path A-X-Γ-Z-A-Γ for optimized WTeS and WTeSe to identify their dynamic stability (See supplementary material). Additionally, the formation energies of both compounds are negative and are

closer to that of the parent Weyl semimetal phase WTe_2, the details of calculations are given in supplementary material. In our electronic structure calculations, we use the generalized gradient approximation (GGA) and density functional theory (DFT). We employ the plane-wave basis set and the projector augmented wave method as implemented in the Vienna *Ab initio* Simulation Package (VASP) [32]. A plane-wave cutoff energy of 500eV, a force convergence criteria of 0.001eV/Å and a Monkhorst-Pack mesh of 10×8×6 are used in the unit cell calculations. All calculations include the vdW correction between interlayers realized by the DFT-D3 scheme [33] and SOC interaction. The topological properties are identified by the Wannier charge center (WCC) and the surface Fermi arc calculations using tight-binding Hamiltonians [10]. The tight-binding matrix was constructed by projecting the Bloch states into maximally localized Wannier functions (MLWFs) in the Wannier90 package [10]. We have generated atomic like Wannier function for W-*s*,*d* and Te/S/Se-*p* orbitals in our calculations. We examine surface states and the Fermi arcs structures on the (001) and (010) surface by considering a half-infinite surface using the iterative Green's function method [9, 34, 35]. The *k*-dependent local densities of states (LDOS) are projected from the half-infinite bulk to the outermost surface unit cell to demonstrate the surface band structures.

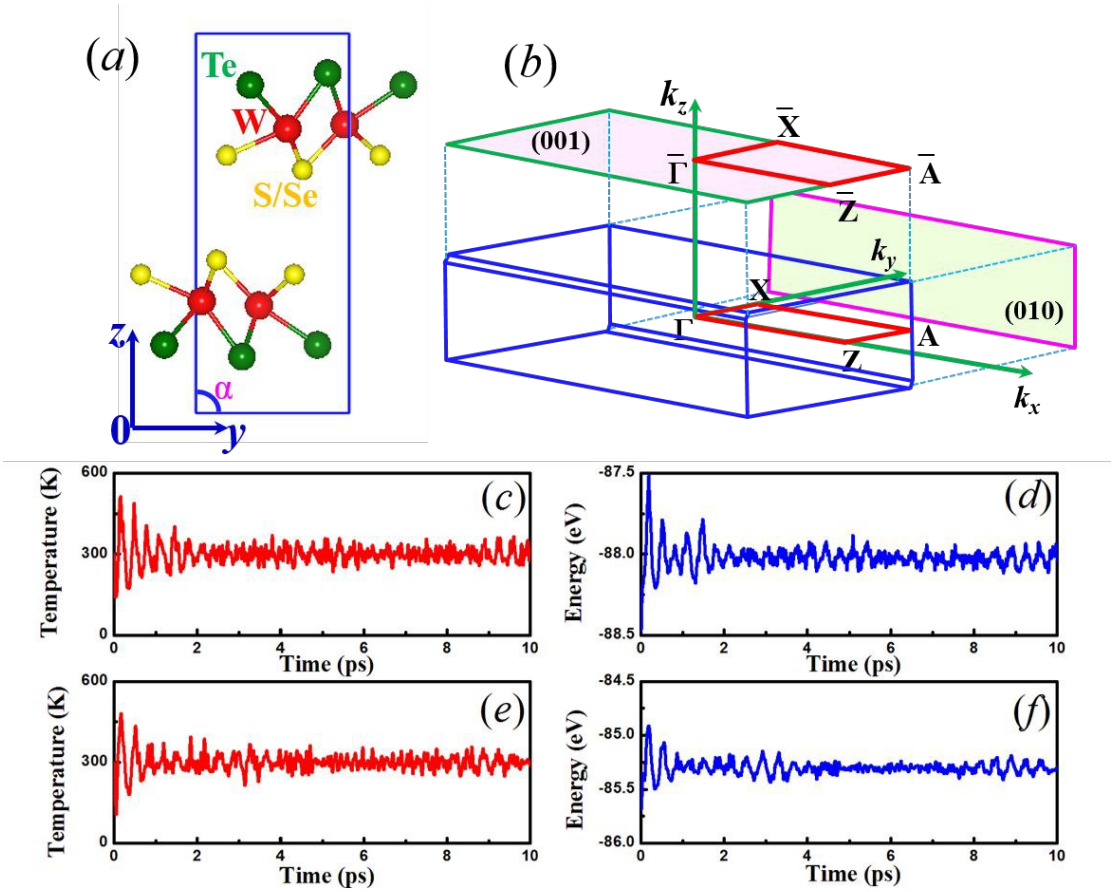

Fig.1 (*a*)The Janus superlattice structures of WTeX (X=S, Se); (*b*) The high symmetry lines in bulk and the (001) and (010) surface Brillouin zone (BZ) for optimized WTeS; (*c*)~(*f*)The temperature and total energy per unit cell as a function of simulation time in FPMD calculations for WTeS ((*c*),(*d*)) and WTeSe ((*e*),(*f*)).

View Article Online
DOI: 10.1039/C9NR04551A

Table I Lattice parameters of T_d-WTe_2 [2] and optimized Janus superlattice structures of WTeS/Se in monoclinic phase with DFT-D3 VdW correction. The values quoted are obtained at plane wave energy cutoff 500eV and a Monkhorst-Pack mesh of 10×8×6 points. The errors for WTeS were computed from the spread in values for results obtained at energy cutoffs 300eV, 350eV, … , 1000eV as well as meshes 10×8×4,10×8×6, 12×8×4, 12×8×6, 12×10×4, 12×10×6,12×10×8.

Systems	a(Å)	b(Å)	c(Å)	α(°)	β=γ(°)
T_d-WTe_2	3.477	6.249	14.018	90.00	90
WTeS	3.321±0.003	6.030±0.003	13.13±0.04	91.81±0.06	90
WTeSe	3.381±0.002	6.122±0.002	13.67±0.03	91.20±0.01	90

3. Results and Discussion

The orbital resolved electronic bands along high symmetry lines A-X-Γ-Z-A-Γ in the Brillouin zone (BZ) for WTeS and WTeSe Janus structures are illustrated in Fig. 2. The bands near the Fermi level consist mainly of W-*d* orbitals and a small number of W-*s*, Te/S/Se-*p* for both WTeS and WTeSe. The DFT-based bands and tight-binding bands have excellent agreement in the range of -1.5eV to 1.5eV near the Fermi level. The large hole pocket at the Γ point and the tiny electron-pockets along the Γ-X line are clearly visible. This is similar to the pristine T_d-WTe_2 and T_d-$MoTe_2$ [2, 3, 19, 20]. The minimal band gaps under SOC are 28meV and 35meV for WTeS and 45meV and 5meV for WTeSe. The bands have no crossing points along the high symmetry line between the CB and the VB. We note that the band touching points deviate from the high symmetry line in the presence of SOC. The possible crossing points can be found near the minigaps by searching the whole BZ based on Wannier tight-binding bands. We observe four twofold degeneracy Weyl points between CB and VB for both WTeS and WTeSe, which is the minimal number of Weyl points in a time reversal invariant system [26].

View Article Online
DOI: 10.1039/C9NR04551A

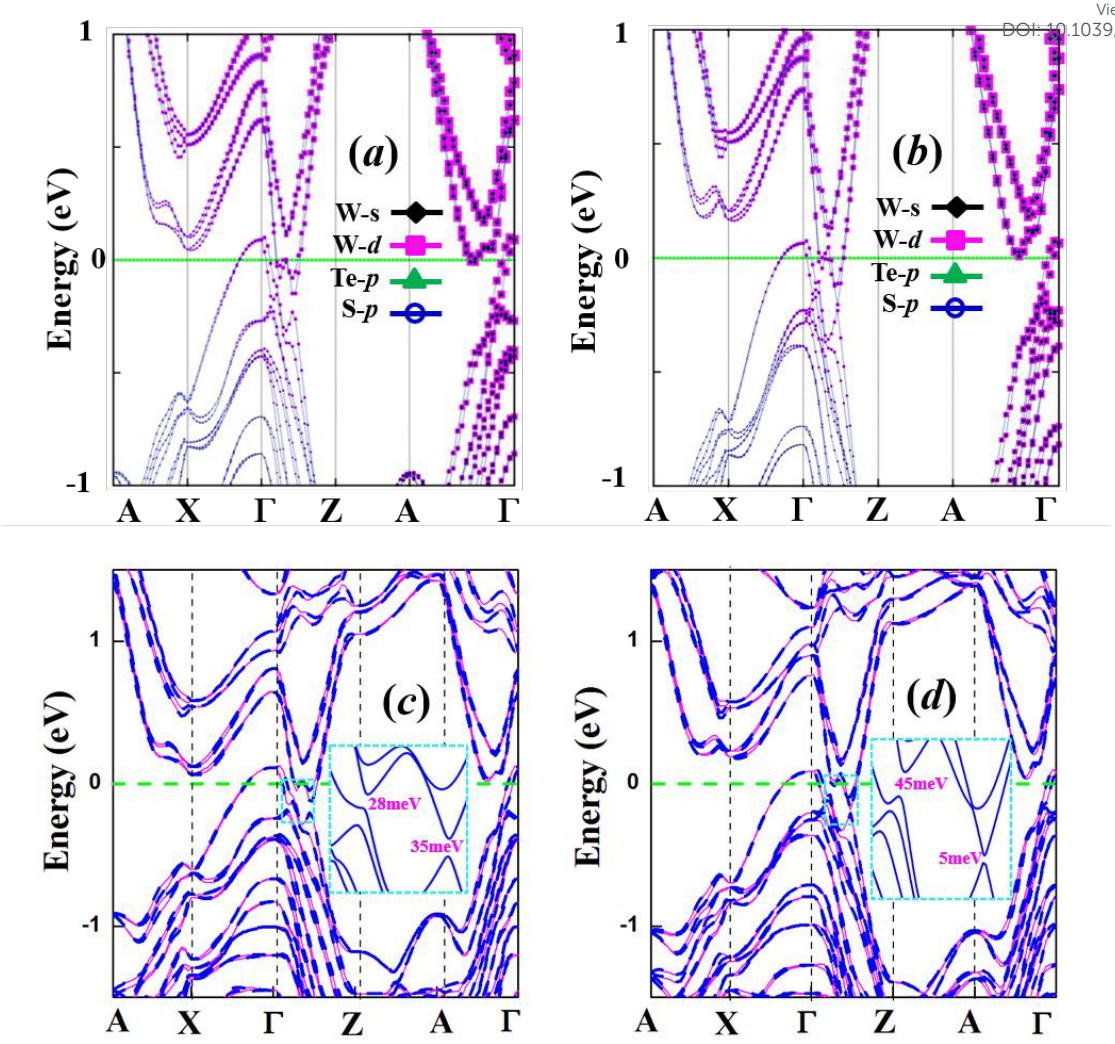

Fig.2 The orbital resolved electronic bands with spin-orbit coupling for (*a*) WTeS and (*b*) WTeSe. The DFT bands (pink) and tight-binding bands (blue) for (*c*) WTeS and (*d*) WTeSe .The green horizontal lines represent Fermi level. The insets show the bands with minigaps.

To verify topological properties, we firstly locate the positions of band touching points between CB and VB based on the tight-binding Hamiltonians. The number of Weyl nodes is four and the corresponding energies for all Weyl points are close to -126.5meV and -97.2meV for WTeS and WTeSe, respectively, as listed in Table II. The results are different in several aspects compared to those of pristine WTe_2 and its analogous compound $MoTe_2$. Firstly, the Weyl points are positioned below the Fermi level which is within in the range of observation by traditional ARPES measurements. In distinction, the Weyl nodes in the pristine T_d-WTe_2 (52meV, 58meV) [2], $MoTe_2$ (55meV) [3, 19] or doping system $Mo_xW_{1-x}Te$ (~50meV) [20] are all located above the Fermi level which requires pump probe ARPES technique to be observed [26].

Table II The positions of Weyl points (WP) in reduced coordinates, energy compared to Fermi level and the corresponding Chern number (*C*) for optimized WTeS and WTeSe for plane wave energy cutoff 500eV and mesh of 10×8×6 *k*-points. The 3-digit accuracy reflects small changes between

View Article Online
DOI: 10.1039/C9NR04551A

cutoffs 500eV and 700eV.

Systems	WP	$k_x(2\pi/a)$	$k_y(2\pi/b)$	$k_z(2\pi/c)$	E-E_f (eV)	C
WTeS	WP1	0.207	0.026	0.269	-0.127	+1
	WP2	0.207	-0.027	-0.270	-0.126	-1
	WP3	-0.207	0.027	0.270	-0.126	-1
	WP4	-0.207	-0.026	-0.269	-0.127	+1
WTeSe	WP1	0.141	0.002	-0.488	-0.098	+1
	WP2	0.141	-0.002	-0.489	-0.097	-1
	WP3	-0.141	-0.002	0.488	-0.097	-1
	WP4	-0.141	0.002	-0.489	-0.098	+1

Secondly, the number of Weyl points is four which is the minimal number allowed in a time reversal symmetric system. This minimum number of Weyl nodes will greatly simplify the experimental measurements. It is worth noting that the four Weyl nodes are located in four different quadrants of first BZ as plotted in Fig.3 (*a*) and (*d*). This markedly different distribution makes it a generic momentum semimetal (GMSM) in the extensive classification of topological materials [5] and results in surface Fermi arcs in the (010) surface in addition to the (100) surface. The four Weyl points also demonstrate a central inversion (time reversal) symmetry c_i and an M_x reflection symmetry. The (100) projection of the Weyl nodes with opposite chirality is in the same position on the (100) plane. This leads to complicated or invisible Fermi arcs. The large separation of Weyl nodes and the large length of Fermi arcs increase significantly the topological strength of the systems [20]. The reciprocal distances along the k_z (k_y) direction between the two opposite chirality Weyl points WP1/WP2 and WP3/WP4 are approximately close to $0.54|G_z|$ ($0.05|G_y|$) and $0.70|G_z|$($0.02|G_y|$), where $|G_z|=|2\pi/c|$ ($|G_y|=|2\pi/b|$) is the length of the reciprocal lattice vector along the k_z (k_y) direction. We note that the corresponding separation distances are around 0.007 (WTe_2), 0.042 ($MoTe_2$) and 0.04 ($Mo_{0.4}W_{0.6}Te$) in units $|2\pi/b|$ [2, 3, 19, 20]. All Weyl nodes are located away from the k_z=0 plane which is different from the conventional T_d-phase structure due to broken non-symmorphic space g_{xz} symmetry [2]. The basic reason is the lack of rotation symmetry along the z axis for the optimized Janus structure. The relatively large separation together with few bands crossing the Fermi level in WTeS/Se should make the Weyl nodes to be readily observable in ARPES experiments.

View Article Online
DOI: 10.1039/C9NR04551A

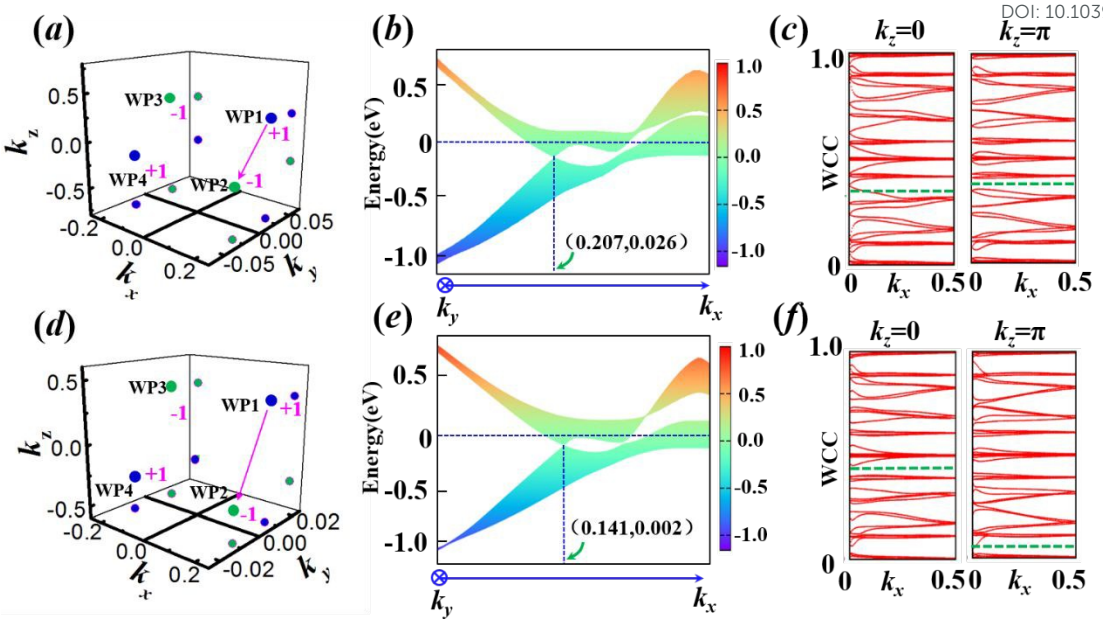

Fig.3 The Weyl nodes, the 2D band dispersion and the Wannier charge center for WTeS (*a*)-(*c*) and WTeSe (*d*)-(*f*).The 2D dispersions are calculated in the k_z=0.267 and 0.353 planes in units of $2\pi/c$, respectively. The big blue and green dots represent Weyl nodes with positive and negative chirality, and the small dots represent the protective positions of bulk Weyl nodes in the k_x-k_y and k_z-k_x plane in figure (*a*) and (*d*). The blue horizontal and vertical lines in figure (*b*) and (*e*) represent Fermi level and the k_x coordinate of Weyl point in reduced coordinate respectively. Note that the k_y axis is perpendicular to the page. (*c*)(*f*)The evolution of WCC in two time-reversal invariant planes k_z=0, π. The WCC intersects arbitrary reference line an odd number of times in k_z=0 (WTeS) and k_z=π (WTeSe) planes and give a nontrivial Z_2 number of 1. The green dash lines in figure (*c*) and (*f*) are arbitrary reference positions.

Thirdly, the linear dispersion around a Weyl point shows point-like feature in momentum space and form a closed point-like Fermi surface which is a manifest of type I Weyl point as illustrated in Fig.3 (*b*) (*e*) (see supplementary materials). The touching points between CB and VB are located at -0.127eV and -0.098eV. The chirality of the Weyl nodes, corresponding to a magnetic monopole in momentum space, has the topological character of a Weyl node and can be calculated by integrating the surface surrounding the touching point [2, 3, 34]. Consequently, the Weyl cones demonstrate a typical characteristic feature of a type-I Weyl semimetal for both Janus structures, WTeS/WTeSe, as demonstrated by the broken inversion symmetry of the TaAs family with 12 pairs of Weyl points [1, 8]. This is a significant difference compared to standard T_d-WTe_2/$MoTe_2$ which is typical a type II Weyl semimetal. The result implies the possibility of realizing a phase transition from Type II to Type I Weyl semimetal by doping WTe_2.

The topological characteristic of the Weyl node can also be connected with a Z_2 invariant which is usually used for a TI. For 2D materials stacked along the *z* axis, a nonzero Z_2 at just the k_z=0 plane shows a non-trivial topological number. All Weyl points are located in the $k_z \neq 0, \pi$ planes and this results in an insulating gap between

View Article Online
DOI: 10.1039/C9NR04551A

CB and VB in the k_z=0, π planes. The Wilson loop (WCC) can be calculated by integrating along k_y at fixed k_x in two time-reversal invariant planes k_z=0 and k_z=π and the results are shown in Fig. 3 (*c*) and (*f*). For WTeS, The evolution of WCC shows one band crossing green dash line (k_z=0 plane) and no band crossing the green dash line (k_z=π plane). As a result, the corresponding Z_2 invariant equal 1 and 0 on k_z=0 and k_z=π plane, respectively. The Wilson loop gives Z_2 invariants as 1 at the k_z=0 (WTeS) and k_z=π (WTeSe) planes and identifies their topological feature of bands. The topological property of materials generally give rise to characteristic surface states associated with a surface Fermi arc between surface projective points of bulk Weyl nodes.

The characteristic surface states and Fermi arcs on the (001) and (010) surface are calculated by implementing a recursive Green function method for the Wannier-based tight-binding Hamiltonians [9, 35]. The Fermi surface in the (001)/(010) planes and the band dispersion along a line cutting through a pair of Weyl nodes, WP1 and WP2, are shown in Fig. 4 and Fig. 5, respectively. The surface projective points of bulk Weyl nodes are also denoted using blue (positive chirality) and green (negative chirality) dots. For both WTeS and WTeSe, the (001) surface exhibits many larger hole pockets around the Γ point and a tiny electron pocket along the Γ-X line which agrees with the results of the electronic bands as shown in Fig. 2 (*a*). The two (001) surface Fermi arcs connecting WP1 and WP2 are clearly visible. The Fermi arc starts from a projective point and ends in another one with opposite chirality. These simple arc structures simplify the analysis of the Weyl fermion physics in the transport measurement. The separation distance in the (010) projective surface are $0.54|G_z|$ (0.261/Å) and $0.70|G_z|$ (0.32/Å) for WTeS and WTeSe, respectively, which is the order of magnitude of the reciprocal vector. We note that the Fermi arc on the (010) surface for WTeS is merged into the surface of the bulk states as shown in Fig. 4 (*b*). This may be related to the surface projection pattern of Weyl nodes which is dependent on the surface potential and the atom structures at the surface [1, 20]. The Fermi arc is completely integrated into the surface projection of bulk states in the (001) surface for WTeS as illustrated in Fig. 5 (*a*). In contrast, a Fermi arc that approximates a flat band is clearly visible in the bottom $(00\bar{1})$ surface in Fig.5 (*b*). The (010) surface arcs in Fig.(*c*)(*d*) show a different flatness of the Fermi arc compared to that of the (001) surface in Fig.(*a*) and (*b*) for WTeS. These surface-dependent Fermi arcs appear in the surface band dispersion of WTeSe as shown in Fig. 5 (*e*)-(*h*). Interestingly, the Fermi arc displays a "continuous" arc structure: a Fermi arc (ss2) links two WPs in the same BZ in the (010) surface whereas another Fermi arc (ss1) links two WPs in an adjacent periodic BZ in the $(0\bar{1}0)$ surface as illustrated in Fig. 5 (*g*)-(*h*). Two arcs with different lengths form a closed continuous loop which is quite different from a conventional Fermi arc structure. For example, the Fermi arc in two (001) surfaces links two Weyl points that are located in the same BZ for the TaAs family [1, 8, 15]. The unique connection mode of the surface Fermi arc may lead to exotic electronic transport properties and we expect a verification of such effects in future experiments.

View Article Online
DOI: 10.1039/C9NR04551A

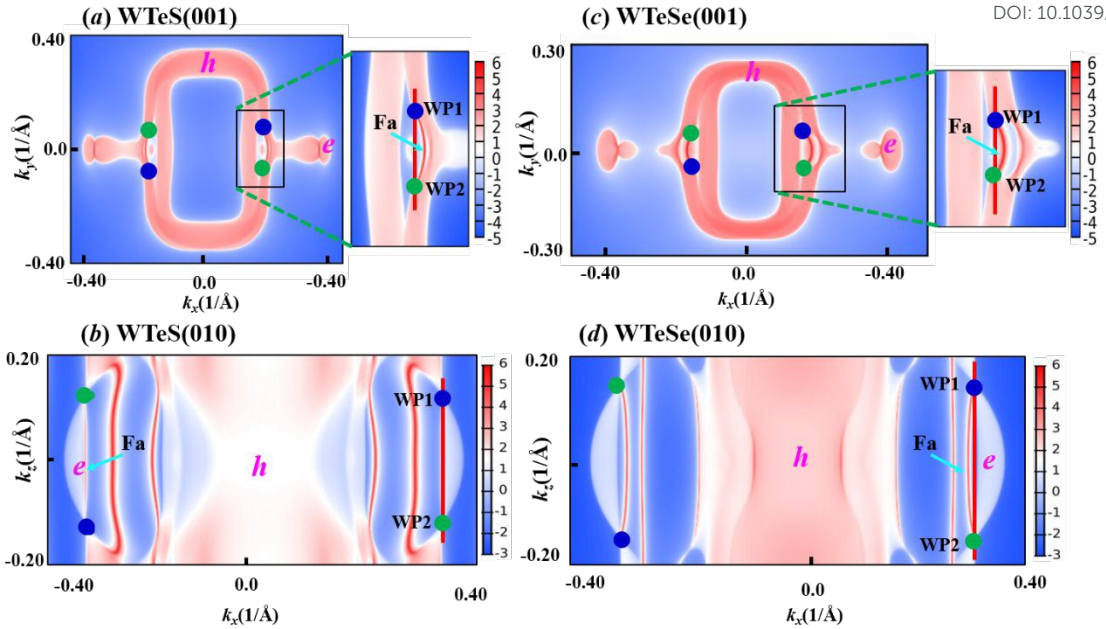

Fig.4 The spectral function of the (001) surface ((*a*) (*c*)) and (010) surface ((*b*) (*d*)) for WTeS and WTeSe. The blue and green points represent projective Weyl nodes with positive and negative chirality respectively. The red line shows a cut line connecting two Weyl nodes. The *h* and *e* represent electron and hole pockets, respectively. The color stands for the natural logarithm of the density of state.

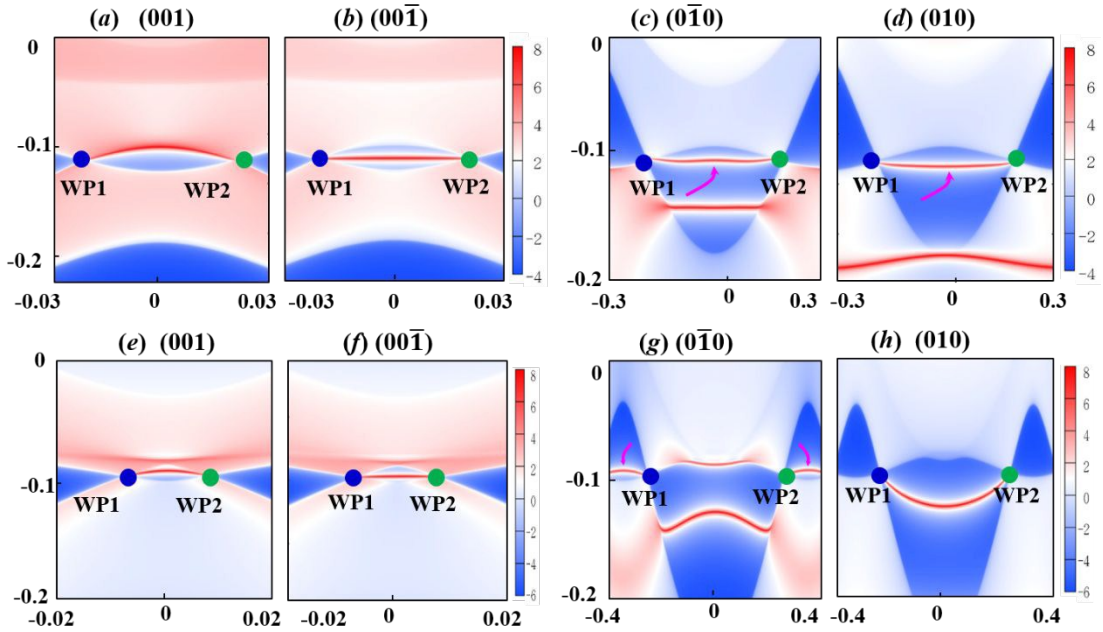

Fig.5 The (001) and (010) surface and bulk projective bands of (*a*)-(*d*) WTeS and (*e*)-(*h*) WTeSe along surface momentum space cut lines in unit 2π/*c* as shown in Fig. 4. The magenta arrow is placed to point the surface Fermi arcs. Other Fermi arc between WP1 and WP2 is shown in deep red line. The color stands for the natural logarithm of the density of state.

In order to check the robustness of topological properties, we further study the electronic state under uniaxial strain along *c* axis for both systems. The applied strain varies from compressive -10% to tensile 10% strain. The Weyl node's distributions and

View Article Online
DOI: 10.1039/C9NR04551A

phase diagrams for both systems are plotted in Fig. 6. For WTeS, the four Weyl nodes remain present in a wide strain range from compression -6% to tensile 8%. Moreover, the four Weyl points with an M_x and c_i symmetry are distributed in the same quadrant of the BZ as the strain-free WTeS. The robustness of the Weyl points against external strain is larger than for the pristine T_d-WTe_2 and its analogous compounds. The 2% strain will lead to the annihilation of a pair of Weyl points or a transition from type I to Type II node in T_d-WTe_2/$MoTe_2$ [2, 3]. The drastic change under small strain for the Weyl points makes pristine T_d-WTe_2/$MoTe_2$ a fragile topological material even for small lattice compression or expansion at the evaluated temperature. The k_x coordinates of the Weyl points under strain are basically unchanged. However, the k_y coordinates have a significant change from ~0.8 % (tensile 8%) to 5% (compression 5%) in units of $2\pi/b$. As a result, the maximal length of the Fermi arc goes up to $0.88\times|2\pi/c|$ (tensile 8%) in the (010) surface which is easily observable in an ARPES experiment. Also, the energies of the four Weyl points are basically identical and gradually approach the Fermi level from compressive to tensile strain as shown in Fig. 6 (*b*). In addition, the WTeS transforms into a TI at tensile strain greater than 8% and to a normal metal at compressive strain less than 6%. In the normal metal, there is a large number of energy touching points distributed in the whole BZ.

For WTeSe, the Weyl semimetal state is stable under tensile strain ranging from 0% to 5%. The four Weyl nodes are also located in four different quadrants which are similar to the strain-free case. However, the motion of the Weyl nodes under strain displays a more complicated behavior. For example, the k_y coordinates of the Weyl points firstly move away from the k_x-k_z plane and reach a maximal value $k_y=0.01\times|2\pi/b|$ around tensile strain 2%. Then the Weyl points again approach the k_x-k_z plane as the tensile strain increases further. The Weyl nodes with opposite handedness annihilate each other at about 5% strain and WTeSe transforms into a TI. The system then retains the TI state under tensile strain from 5% to 10%. Notably, the WTeSe is in a compensation semimetal (CSM) phase under compression from -10%-0% which differs from the situation in WTeS. A CSM is a semimetal with direct gap at every *k* point but lacks a full gap in the whole BZ [5].

View Article Online
DOI: 10.1039/C9NR04551A

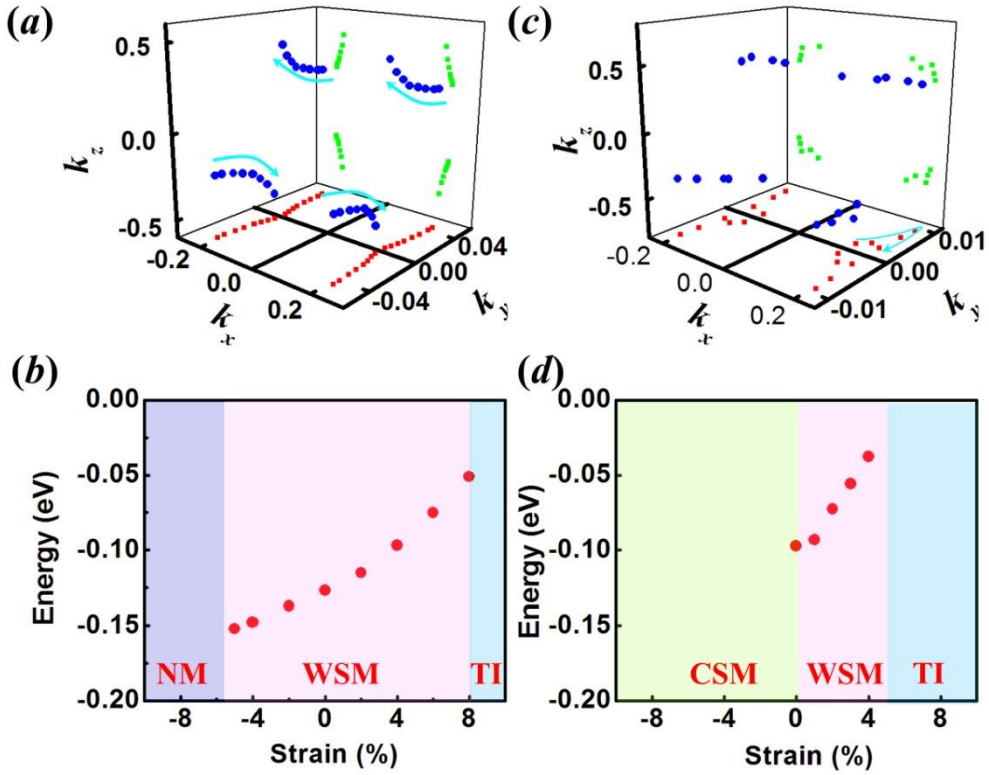

Fig.6 The distribution of Weyl nodes in momentum space under strain for (*a*) WTeS; (*c*) WTeSe. The energy of Weyl nodes and phase diagram under strain for (*b*) WTeS; (*d*) WTeSe. The cyan arrows in (*a*) and (*c*) represent the position change of Weyl points when changing strain from negative compression to positive tensile strain. The red and green dots in (*a*) (*c*) are projections of Weyl points on the k_x-k_y and k_x-k_z planes, respectively.

4. Conclusions

In the present paper, by substituting the Te atom layer with S in the pristine T_d phase of WTe_2, we constructed two Janus superlattice structures WTeS and WTeSe. The thermal stability of the optimized structures is checked by employing first-principles molecular dynamics at 300K. The topological electronic properties are investigated using first-principles calculations and tight-binding Hamiltonians obtained by projecting Bloch bands to Wannier bands. The Weyl points, surface states and Fermi arcs of both Janus structures are identified. Our calculations reveal that both WTeS and WTeSe are Type-I Weyl semimetals with only four Weyl nodes in the BZ. This is a minimal number in a time reversal symmetry system [26] and makes these materials a great platform to study the topological properties when compared to the TaAs Weyl semimetal family [1, 13, and 14]. The four Weyl nodes are located in four different quadrants of the BZ and possess approximately the same energy below the Fermi level. Consequently, they should be accessible by conventional ARPES measurements. Interestingly, the separation of Weyl points in reciprocal space, and the length of the

Fermi arc in the (010) surface state, is on the order magnitude of the reciprocal lattice vector $|G_z|$ and hence might also be observed in ARPES measurements. In addition, we checked the robustness of the topological properties for both systems under uniaxial strain along the stacking direction. The calculations demonstrate that the Weyl semimetal state remains in a wider strain range from -5% (compression) to 8% (tensile) and is more robust than that of the analogous compounds T_d-WTe_2/$MoTe_2$ [2, 3, 19]. Our findings may provide the possibility of designing experimentally a novel type of topological material with Janus-like superlattice structure. These results are important to study the basic physics of Weyl fermions and helpful for realizing possible applications of Weyl semimetal in future topological electronic devices.

Acknowledgements

This work is supported by the National Natural Science Foundation of China (Grant No. 11204261), National Natural Science Foundation of Hunan Province (Grant No. 2018JJ2381) and by a Scholarship of the Hunan Provincial Department of Education (Grant No.2017003). L.J. Meng would like to thank the Physics Theory Group at The University of Warwick for hospitality during a sabbatical stay in 2018-19. We thank Dr Jasmine Desmond for a careful reading of the manuscript.

References

1. Weng, H.; Fang, C.; Fang, Z.; Bernevig, B. A.; Dai, X., *Physical Review X* **2015,** *5* (1). DOI 10.1103/PhysRevX.5.011029.

2. Soluyanov, A. A.; Gresch, D.; Wang, Z.; Wu, Q.; Troyer, M.; Dai, X.; Bernevig, B. A., *Nature* **2015,** *527* (7579), 495-8. DOI 10.1038/nature15768.

3. Wang, Z.; Gresch, D.; Soluyanov, A. A.; Xie, W.; Kushwaha, S.; Dai, X.; Troyer, M.; Cava, R. J.; Bernevig, B. A., *Phys Rev Lett* **2016,** *117* (5), 056805. DOI 10.1103/PhysRevLett.117.056805.

4. Yan, B.; Felser, C., *Annual Review of Condensed Matter Physics* **2017,** *8* (1), 337-354. DOI 10.1146/annurev-conmatphys-031016-025458.

5. Zhang, T.; Jiang, Y.; Song, Z.; Huang, H.; He, Y.; Fang, Z.; Weng, H.; Fang, C., *Nature* **2019,** *566* (7745), 475-479. DOI 10.1038/s41586-019-0944-6.

6. Vergniory, M. G.; Elcoro, L.; Felser, C.; Regnault, N.; Bernevig, B. A.; Wang, Z., *Nature* **2019,** *566* (7745), 480-485. DOI 10.1038/s41586-019-0954-4.

7. Tang, F.; Po, H. C.; Vishwanath, A.; Wan, X., *Nature* **2019,** *566* (7745), 486-489. DOI 10.1038/s41586-019-0937-5.

8. Huang, S. M.; Xu, S. Y.; Belopolski, I.; Lee, C. C.; Chang, G.; Wang, B.; Alidoust, N.; Bian, G.; Neupane, M.; Zhang, C.; Jia, S.; Bansil, A.; Lin, H.; Hasan, M. Z., *Nat Commun* **2015,** *6*, 7373. DOI 10.1038/ncomms8373.

9. Sancho, M. P. L.; Sancho, J. M. L.; Rubio, J., *Journal of Physics F: Metal Physics* **1984,** *14*, 1205-1215.

10. Mostofi, A. A.; Yates, J. R.; Pizzi, G.; Lee, Y.-S.; Souza, I.; Vanderbilt, D.; Marzari, N., *Computer Physics Communications* **2014,** *185* (8), 2309-2310. DOI 10.1016/j.cpc.2014.05.003.

11. Hasan, M. Z.; Kane, C. L., *Reviews of Modern Physics* **2010,** *82* (4), 3045-3067. DOI 10.1103/RevModPhys.82.3045.

12. Zhang, H.; Liu, C.-X.; Qi, X.-L.; Dai, X.; Fang, Z.; Zhang, S.-C., *Nature Physics* **2009,** *5* (6), 438-442.

DOI 10.1038/nphys1270.

13. Xu, G.; Weng, H.; Wang, Z.; Dai, X.; Fang, Z., *Phys Rev Lett* **2011,** *107* (18), 186806. DOI 10.1103/PhysRevLett.107.186806.

14. Wan, X.; Turner, A. M.; Vishwanath, A.; Savrasov, S. Y., *Physical Review B* **2011,** *83* (20). DOI 10.1103/PhysRevB.83.205101.

15. Jia, S.; Xu, S. Y.; Hasan, M. Z., *Nat Mater* **2016,** *15* (11), 1140-1144. DOI 10.1038/nmat4787.

16. Huang, S. M.; Xu, S. Y.; Belopolski, I.; Lee, C. C.; Chang, G.; Chang, T. R.; Wang, B.; Alidoust, N.; Bian, G.; Neupane, M.; Sanchez, D.; Zheng, H.; Jeng, H. T.; Bansil, A.; Neupert, T.; Lin, H.; Hasan, M. Z., *Proc Natl Acad Sci U S A* **2016,** *113* (5), 1180-5. DOI 10.1073/pnas.1514581113.

17. Xu, S.-Y.; Belopolski, I.; Alidoust, N.; Neupane, M.; Bian, G.; Zhang, C.; Sankar, R.; Chang, G.; Yuan, Z.; Lee, C.-C.; Huang, S.-M.; Zheng, H.; Ma, J.; Sanchez, D. S.; Wang, B.; Bansil, A.; Chou, F.; Shibayev, P. P.; Lin, H.; Jia, S.; Hasan, M. Z., *Science* **2015,** *349*.

18. Johansson, A.; Henk, J.; Mertig, I., *Physical Review B* **2019,** *99* (7). DOI 10.1103/PhysRevB.99.075114.

19. Sun, Y.; Wu, S.-C.; Ali, M. N.; Felser, C.; Yan, B., *Physical Review B* **2015,** *92* (16). DOI 10.1103/PhysRevB.92.161107.

20. Chang, T. R.; Xu, S. Y.; Chang, G.; Lee, C. C.; Huang, S. M.; Wang, B.; Bian, G.; Zheng, H.; Sanchez, D. S.; Belopolski, I.; Alidoust, N.; Neupane, M.; Bansil, A.; Jeng, H. T.; Lin, H.; Zahid Hasan, M., *Nat Commun* **2016,** *7*, 10639. DOI 10.1038/ncomms10639.

21. Autes, G.; Gresch, D.; Troyer, M.; Soluyanov, A. A.; Yazyev, O. V., *Phys Rev Lett* **2016,** *117* (6), 066402. DOI 10.1103/PhysRevLett.117.066402.

22. Chang, G., *Sci. Adv.* **2016**.

23. Li, P.; Wen, Y.; He, X.; Zhang, Q.; Xia, C.; Yu, Z. M.; Yang, S. A.; Zhu, Z.; Alshareef, H. N.; Zhang, X. X., *Nat Commun* **2017,** *8* (1), 2150. DOI 10.1038/s41467-017-02237-1.

24. Wang, Y.; Liu, E.; Liu, H.; Pan, Y.; Zhang, L.; Zeng, J.; Fu, Y.; Wang, M.; Xu, K.; Huang, Z.; Wang, Z.; Lu, H. Z.; Xing, D.; Wang, B.; Wan, X.; Miao, F., *Nat Commun* **2016,** *7*, 13142. DOI 10.1038/ncomms13142.

25. Li, Y.; Gu, Q.; Chen, C.; Zhang, J.; Liu, Q.; Hu, X.; Liu, J.; Liu, Y.; Ling, L.; Tian, M.; Wang, Y.; Samarth, N.; Li, S.; Zhang, T.; Feng, J.; Wang, J., *Proc Natl Acad Sci U S A* **2018,** *115* (38), 9503-9508. DOI 10.1073/pnas.1801650115.

26. Belopolski, I.; Yu, P.; Sanchez, D. S.; Ishida, Y.; Chang, T. R.; Zhang, S. S.; Xu, S. Y.; Zheng, H.; Chang, G.; Bian, G.; Jeng, H. T.; Kondo, T.; Lin, H.; Liu, Z.; Shin, S.; Hasan, M. Z., *Nat Commun* **2017,** *8* (1), 942. DOI 10.1038/s41467-017-00938-1.

27. Lu, A. Y.; Zhu, H.; Xiao, J.; Chuu, C. P.; Han, Y.; Chiu, M. H.; Cheng, C. C.; Yang, C. W.; Wei, K. H.; Yang, Y.; Wang, Y.; Sokaras, D.; Nordlund, D.; Yang, P.; Muller, D. A.; Chou, M. Y.; Zhang, X.; Li, L. J., *Nat Nanotechnol* **2017,** *12* (8), 744-749. DOI 10.1038/nnano.2017.100.

28. Ji, Y.; Yang, M.; Lin, H.; Hou, T.; Wang, L.; Li, Y.; Lee, S.-T., *The Journal of Physical Chemistry C* **2018,** *122* (5), 3123-3129. DOI 10.1021/acs.jpcc.7b11584.

29. Shi, W.; Fan, K.; Wang, Z., *Phys Chem Chem Phys* **2018,** *20* (46), 29423-29429. DOI 10.1039/c8cp03354d.

30. Ma, Y.; Kou, L.; Huang, B.; Dai, Y.; Heine, T., *Physical Review B* **2018,** *98* (8). DOI 10.1103/PhysRevB.98.085420.

31. Lin, J.; Zhou, J.; Zuluaga, S.; Yu, P.; Gu, M.; Liu, Z.; Pantelides, S. T.; Suenaga, K., *ACS Nano* **2018,** *12* (1), 894-901. DOI 10.1021/acsnano.7b08782.

32. Kresse, G.; Furthmu¨ller, J., *PHYSICAL REVIEW B* **1996,** *54*, 11169.

33. Grimme, S.; Antony, J.; Ehrlich, S.; Krieg, H., *J Chem Phys* **2010,** *132* (15), 154104. DOI 10.1063/1.3382344.

34. Wu, Q.; Zhang, S.; Song, H.-F.; Troyer, M.; Soluyanov, A. A., *Computer Physics Communications* **2018,** *224*, 405-416. DOI 10.1016/j.cpc.2017.09.033.

35. Sancho, M. P. L.; Sancho, J. M. L.; Rubio, J., *Journal of Physics F: Metal Physics* **1985,** *15*, 851-858.